Editors' Suggestion

Possible Spin-Triplet Excitonic Insulator in the Ultraquantum Limit of $HfTe_5$

Jinyu Liu,[1] Varsha Subramanyan,[2,3] Robert Welser,[1] Timothy McSorley,[1] Triet Ho,[4] David Graf,[5] Michael T. Pettes,[3] Avadh Saxena,[2] Laurel E. Winter,[6] Shi-Zeng Lin,[2,3] and Luis A. Jauregui[1,*]

[1]*Department of Physics and Astronomy, University of California, Irvine, California 92697, USA*
[2]*Theoretical Division T-4, Los Alamos National Laboratory, Los Alamos, New Mexico 87545, USA*
[3]*Center for Integrated Nanotechnologies, Los Alamos National Laboratory, Los Alamos, New Mexico 87545, USA*
[4]*Department of Mechanical and Aerospace Engineering, University of California, Irvine, California 92697, USA*
[5]*National High Magnetic Field Laboratory, Florida State University, Tallahassee, Florida 32310, USA*
[6]*National High Magnetic Field Laboratory, Los Alamos National Laboratory, Los Alamos, New Mexico 87544, USA*

(Received 10 December 2024; accepted 16 June 2025; published 22 July 2025)

More than 50 years ago, excitonic insulators formed by the pairing of electrons and holes due to Coulomb interactions were first predicted [A. N. Kozlov and L. A. Maksimov, Sov. J. Exp. Theor. Phys. **21**, 790 (1965); L. V. Keldysh and Y. V. Kopaev, Sov. Phys. Solid State **6**, 2219 (1965); D. Jérome, T. M. Rice, and W. Kohn, Phys. Rev. **158**, 462 (1967)]. Since then, excitonic insulators have been observed in various classes of materials, including quantum Hall bilayers, graphite, transition metal chalcogenides, and more recently in moiré superlattices. In these excitonic insulators, an electron and a hole with the same spin bind together, and the resulting exciton is a spin singlet. Here, we report the experimental observation of a spin-triplet excitonic insulator in the ultra-quantum limit of a three-dimensional topological material $HfTe_5$. We observe that the spin-polarized zeroth Landau bands dispersing along the field direction cross each other beyond a characteristic magnetic field in $HfTe_5$, forming the one-dimensional Weyl mode. Transport measurements reveal the emergence of a gap of about 250 μeV when the field surpasses a critical threshold. By performing the material-specific modeling, we identify this gap as a consequence of a spin-triplet exciton formation, where electrons and holes with opposite spin form bound states, and the translational symmetry is preserved. The system reaches charge neutrality following the gap opening, as evidenced by the zero Hall conductivity over a wide magnetic field range (10–72 T). Our finding of the spin-triplet excitonic insulator paves the way for studying novel spin transport including spin superfluidity, spin Josephson currents, and Coulomb drag of spin currents in analogy to the transport properties associated with the layer pseudospin in quantum Hall bilayers.

DOI: 10.1103/bj2n-4k2w

Introduction—At high magnetic fields (B), the motion of charged particles within two-dimensional (2D) or three-dimensional (3D) systems becomes quantized into discrete energy levels known as Landau levels (LLs). As B increases, the system reaches the quantum limit (QL), where charge carriers primarily occupy the lowest LL(s), or the zeroth LL(s) in the case of relativistic fermions. In this regime, quenched kinetic energy and a significantly enhanced density of states (DOS) give rise to exotic phenomena. In 2D, the interplay between electron-electron interactions and the topological nature of LLs can lead to correlated electronic phases, including Wigner crystals [1], charge density waves [2,3], excitonic insulators [4,5], and the fractional quantum Hall effect [6,7]. In 3D, while the energy-momentum relation remains dispersive along the field direction, the electron motion perpendicular to B is confined, effectively reducing the dimensionality to one dimensional (1D). This confinement coupled with quenched kinetic energy theoretically promotes interaction-driven instabilities similar to those in 2D systems [8,9]. However, due to the required high fields to reach the ultra-QL in conventional metals, identifying such phases in 3D systems remains challenging, with evidence limited to graphite [10–14] and bismuth [15]. Recent discoveries in topological materials offer new avenues to explore QL phenomena in 3D systems [16–21]. Transition metal pentatellurides, i.e., $(Zr, Hf)Te_5$, have attracted attention due to their nontrivial topological characteristics and unusual transport properties [22–28]. Their small Fermi surfaces make them highly suitable for exploring novel quantum phenomena in the ultra-QL. For instance, as B increases beyond the QL (B_{QL}), the evolution of cyclotron energy and the Landau band (LB) splitting can lead to the zeroth LB crossing. This inter-LB crossing between the zeroth conduction (0^-) and valence (0^+) LLs is particularly guaranteed by the weak topological insulator (WTI) nature because of the unique band inversion parameters, as

*Contact author: lajaure1@uci.edu

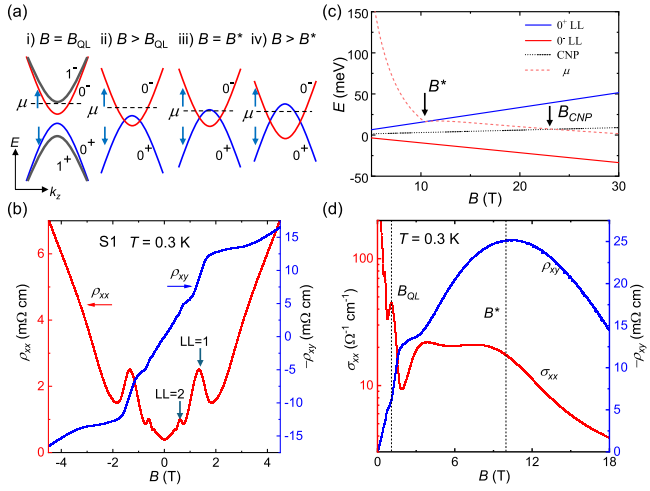

FIG. 1. (a) Schematic of zeroth LBs and chemical potential (μ) under increasing magnetic field (B). (b) ρ_{xx} and ρ_{xy} vs B measured from S1. (c) Schematic of the calculated field dependence of zeroth LBs, μ, and the CNP at $k_z = 0$ for S1. (d) σ_{xx} and $-\rho_{xy}$ vs B. B^* represents the onset of 1D Weyl mode formation, as shown in (a) (iii). σ_{xx} between B_{QL} and B^* is expected to be in a broad minimum, but the impurity scattering [30] and the instability of the fractional quantized Hall plateaus [28] may affect it.

proposed and experimentally demonstrated in $HfTe_5$ by Wu *et al.* [29]. In contrast, the lowest LBs in trivial insulators fan out more with increasing B; meanwhile, those in the strong topological insulator phase only cross with each other in an optimal magnetic field range but become separated beyond a critical field [30]. As illustrated in Fig. 1(a), with large Landé g factors, the Zeeman energy can surpass both the band gap and the Fermi energy, driving the spin-polarized zeroth LBs toward each other. The successive zeroth LB crossing persistently closes the band gap [Fig. 1(a), (ii)]. As the chemical potential (μ) is also modulated by B, beyond a characteristic field B^*, a 1D Weyl mode is created [29–33], effectively generating an anisotropic 1D band structure without geometric confinement [Fig. 1(a), (iii) and (iv)].

Nevertheless, the electronic liquid in 1D systems is well known for its susceptibility to forming various correlated quantum states, which are typically associated with a gap opening in the low-energy excitation spectrum [34]. When μ approaches the 1D Weyl nodes, the enhanced DOS can further promote correlated phenomena. One potential phase that may emerge is the excitonic insulator (EI), as predicted by Kohn in small-gap semiconductors where the exciton binding energy exceeds the band gap. This state forms through a coherent pairing of electrons and holes, exhibiting a charge-neutral Bardeen-Cooper-Schrieffer- (BCS) like condensation [35]. Particularly, spin-triplet EIs can exhibit intriguing magnetic properties, such as spin superfluidity, analogous to spin-triplet superconductivity [36,37] and the superfluidity of ^{3}He [38]. However, achieving such spin-triplet EI remains a significant challenge [39–41]. Interestingly, the electron and hole zeroth LBs in $HfTe_5$ resemble a direct-gap semiconductor with a tunable band gap modulated by B. These spin-polarized zeroth LBs allow the creation of spin-triplet excitons, where the electron and hole bands have opposite spins, enabling a spin-triplet EI phase [39]. Therefore, $HfTe_5$ is an ideal material candidate to explore the magnetic-field-driven spin-triplet EIs or other correlated states. Here, we investigate quantum transport properties in the ultra-QL of low-carrier-density $HfTe_5$ samples, revealing three key phenomena. First, a Lifshitz transition to the 1D Weyl phase occurs as spin-polarized 0^+ and 0^- LBs cross with each other [29,30,33], leading to a negative longitudinal magnetoresistance (NLMR) in the interlayer resistivity (ρ_{zz}). Second, a field-driven metal-to-insulator transition is observed, characterized by a gap opening (~250 μeV), as indicated by intralayer (ρ_{xx}) resistivity and ρ_{zz} measurements, due to instabilities in the 1D electronic liquid. Third, the Hall resistivity (ρ_{xy}) vanishes, demonstrating a charge-neutral state beyond a characteristic field (B_{CNP}), with B_{CNP} exhibiting a BCS-like temperature dependence. This charge-neutral state persists to the highest measured fields. Material-specific modeling suggests that this insulating state arises from electron-hole pairing forming a spin-triplet EI gap at the 1D Weyl nodes, supported by the zero Hall conductivity and nonlinear transport measurements. These findings highlight interaction-driven quantum phenomena in the ultra-QL of $HfTe_5$, advancing our understanding of correlation effects in topological materials.

Results—Our chemical vapor transport grown $HfTe_5$ samples are elongated, beltlike single crystals with an orthorhombic structure belonging to the *cmcm* space group. Previous studies [29,42] have identified pristine $HfTe_5$ as a WTI with a Dirac gap of ~3 meV at the Γ point and highly anisotropic band dispersions along different momentum directions. For the intralayer measurements, current (I) is applied along the a axis with B perpendicular to the a-c plane. Figure 1(b) shows ρ_{xx} and ρ_{xy} vs B at $T = 0.3$ K, for sample 1 (S1). In the low field regime, ρ_{xx} exhibits Shubnikov–de Haas (SdH) oscillations with a frequency of 1.1 T. Meanwhile, ρ_{xy} varies linearly with B, corresponding to an electron density of $\sim 10.2 \times 10^{16}$ cm^{-3}. Similar to the 3D quantum Hall effect observed in $(Zr, Hf)Te_5$ [24,28], ρ_{xy} in our samples displays plateaus with corresponding valleys in ρ_{xx}, allowing the identification of LLs. Beyond $B_{\mathrm{QL}} = 1.3$ T, the system enters the QL, where the first LL is depopulated, and only the zeroth LLs are occupied. The nontrivial Berry's phase extracted from the LL fan diagram indicates that the transport is dominated by Dirac fermions at the Γ point, and the contribution from any sidebands is reduced or negligible (see Supplemental Material [43]) [28,42].

Figure 1(c) shows the calculated evolution of the zeroth LLs, μ, and the charge-neutrality point (CNP) at $k_z = 0$ as function of B. Our simulations suggest that μ crosses the 0^+

LL at ~10 T and the CNP at $B_{CNP} \sim 25$ T, using the carrier density from S1 in good agreement with the experimental result (Fig. S4 in Supplemental Material [43]). Figure 1(d) shows σ_{xx} and ρ_{xy} vs B revealing a broad peak in ρ_{xy} far beyond B_{QL}, coinciding with a peak in σ_{xx} which is proportional to the DOS. The field at this peak, $B^* \sim 10$ T, marks the onset of a hole introduction. For $B > B^*$, as shown in Fig. 1(a), μ crosses both 0^- and 0^+ LBs, and the transport is dominated by the 1D Weyl mode.

To corroborate the existence of 1D Weyl mode transport, we perform interlayer current measurements on another sample, S2, by placing multiple electrodes on the top and bottom surfaces, as shown Fig. 2(a). A uniform current density across the a-c plane is ensured as simulated by the finite element analysis performed with COMSOL Multiphysics [Fig. 2(b)]. Figure 2(c) illustrates the formation of the 1D Weyl state in real space for $B > B^*$. With our measurement setup, the parallel electric (E) and B fields condition is fulfilled by applying I and B both along the sample's b axis, producing imbalanced chirality of 1D Weyl fermions. Figure 2(d) shows ρ_{zz} vs B at different temperatures under pulsed fields. At $T = 0.6$ K, ρ_{zz} rises with B, reaching a peak at $B \sim 9.5$ T. Beyond this field, ρ_{zz} decreases, reaching a minimum around 35 T. The B onset of the NLMR agrees well with the calculated and measured $B^* \sim 10$ T from S1 and S2. Moreover, ρ_{zz} exhibits a $1/B^2$ dependence, as shown by the fitting lines in Fig. 2(d). The NLMR is sensitive to the orientation of B and vanishes when B is tilted beyond 44° (Fig. S3 in Supplemental Material [43]). Therefore, the observed NLMR and the EB-like characteristic, similar to the 3D counterpart, unambiguously demonstrates the existence of the 1D Weyl mode. The NLMR persists up to $T = 10$ K and vanishes at $T = 20$ K, likely due to the occupation of higher LLs at elevated temperatures.

We note that for $B > 40$ T, ρ_{zz} starts to increase with B as shown in Fig. S3(b) of Supplemental Material [43], indicating the presence of a competing mechanism. Additionally, the temperature dependence of ρ_{zz} reveals the sample is insulating for $T < 10$ K at all measured fields. One possible explanation for this behavior is discussed below with the introduction of a correlated gap, leading to the disappearance of the NLMR, similarly observed in known type-I Weyl semimetals such as TaAs [18].

To better characterize the QL transport behaviors, we measured sample S3 characterized by a smaller electron density (~5.18×10^{16} cm^{-3}; see Fig. S2 in Supplemental Material [43]). The SdH oscillations with a frequency of 1.0 T results in $B_{QL} = 0.9$ T. The onset of 1D Weyl mode transport marked by the extremum in ρ_{xy} occurs at $B^* = 6$ T. Furthermore, a metal-to-insulator transition is observed at a critical field $B_C \sim 6$ T, as indicated by ρ_{xx} vs B measured at different temperatures [Supplemental Material Fig. S4(c) [43]]. This metal-to-insulator transition is consistently observed across multiple samples [Supplemental Material Figs. S4 and S7(a) [43]], with B_c decreasing for samples with lower electron densities [Supplemental Material Fig. S8(a) [43]].

S3 was further investigated under pulsed fields (Fig. 3). For $T < 4$ K, ρ_{xx} rapidly increases with B for $B < 20$ T, transitioning to a slower increase at higher fields [Fig. 3(a)].

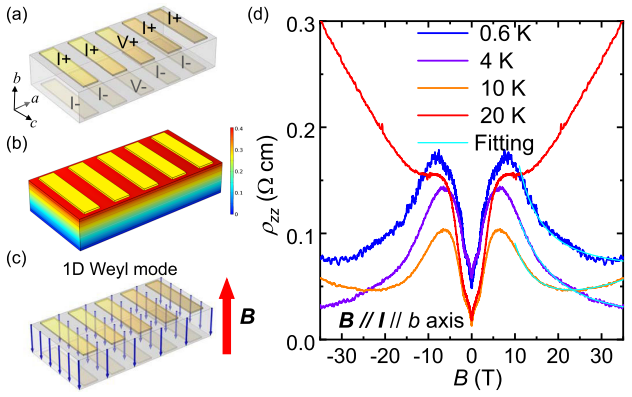

FIG. 2. (a) Schematic of the interlayer resistivity ρ_{zz} measurement used for S2. (b) Finite element analysis simulation of the current density in S2. (c) Schematic of the 1D Weyl mode for $B > B^*$. (d) ρ_{zz} vs B measured at various temperatures with $B//I//b$. The light blue lines represent the fit for the NLMR using $\rho_{zz} \propto 1/B^2$. For $T = 10$ K, the fitting also includes a positive magnetoresistance term proportional to B^2.

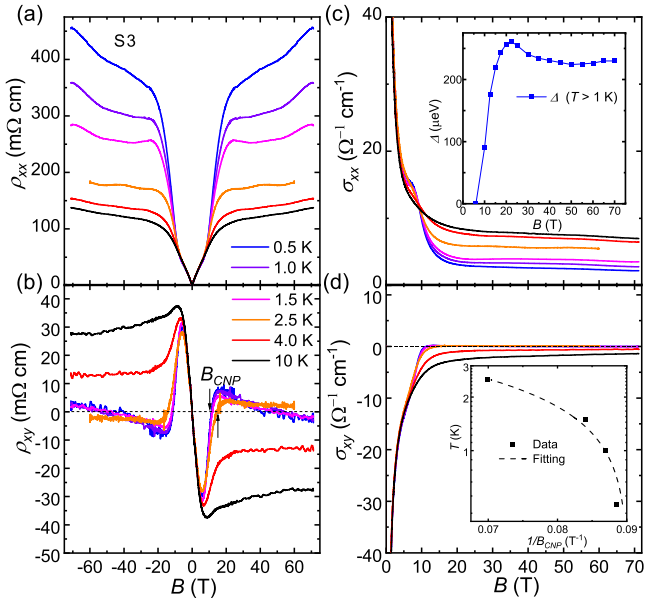

FIG. 3. (a), (b) ρ_{xx} and ρ_{xy} vs B at various temperatures as indicated for S3. (c), (d) σ_{xx} and σ_{xy} vs B obtained from both ρ_{xx} and ρ_{xy}. Inset of (c): activation energy (Δ) vs B extracted from the temperature dependence of ρ_{xx}. Inset of (d): T vs $1/B_{CNP}$. The fitting is described by Eqs. (1) and (2) in Supplemental Material [43].

For ρ_{xy}, deviations from linear field dependence occur beyond B_{QL}, as shown in Fig. 3(b). Remarkably, ρ_{xy} reaches a maximum near $B^* = 6$ T before decreasing rapidly and crossing zero at the CNP around $B_{\mathrm{CNP}} \sim 11$ T. For $B > B_{\mathrm{QL}}$ and $T < 4$ K, ρ_{xy} remains near zero, indicating a transition from electron-dominated behavior at low fields to a state of equal electron-hole density up to $B = 72$ T. However, for $T = 4$ and 10 K, ρ_{xy} does not reach zero, suggesting that the carrier type remains electron dominated at all fields, preventing μ from reaching the CNP. For $B > B_C$, the temperature dependence of ρ_{xx} is well described by the Arrhenius equation $\rho_{xx} \propto \exp(\Delta/2k_BT)$, where the thermal activation energy (Δ) increases with B. Δ reaches ~250 μeV at $B \sim 20$ T and stabilizes around 225 μeV at higher fields [Fig. 3(c) inset].

Longitudinal conductivity ($\sigma_{xx} = [\rho_{xx}/(\rho_{xx}^2 + \rho_{xy}^2)]$) and Hall conductivity ($\sigma_{xy} = [\rho_{xy}/(\rho_{xx}^2 + \rho_{xy}^2)]$) vs B are shown in Figs. 3(c) and 3(d), respectively. σ_{xx} decreases rapidly with decreasing T, consistent with the insulating behavior activated above B_c. σ_{xy} also decreases rapidly for $B > B_c$ and $T < 4$ K, reaching zero at B_{CNP} and remaining near zero up to $B = 72$ T, demonstrating a zero Hall conductivity. The temperature dependence of $B\sigma_{xy}/e$ provides insights into the carrier density difference ($n_e - n_h = B\sigma_{xy}/e$) derived from a semiclassical two-band model (see Appendix A) [14]. For $B > B_{\mathrm{CNP}}$, $B\sigma_{xy}/e$ transitions from electron-dominated to charge-neutral transport for $T < 4$ K. Interestingly, B_{CNP} measured using both pulsed [Fig. 3(d) inset] and superconducting magnets [Supplemental Material Fig. S8(b) [43]], exhibits a strong temperature dependence well described by a BCS-like equation, indicating an excitonic bound state of electrons and holes from the zeroth LLs (see Supplemental Material [43]) [14,44].

Previously, the magnetic-field-induced metal-insulator transition in $ZrTe_5$ was attributed to charge-density-wave (CDW) formation driven by electron-phonon interactions [24,45] or a disorder-driven carrier freeze-out [46]. However, to explain our observations, we propose a model incorporating an excitonic instability, as detailed below.

In the QL, the effective dimension of the system becomes 1D. It is well known that the electron interaction in 1D is nonperturbative. For instance, the Fermi liquid is replaced by Luttinger liquid for an arbitrarily weak interaction. Luttinger liquid is a critical phase that is susceptible to gap opening. Such a gap opening is highly expected when μ is swept around the Weyl nodes, where Van Hove singularities exist at the top and bottom of the valence or conduction band.

The low-energy model [47–50] for $HfTe_5$ is

$$\mathscr{H}(k) = v\left(k_x\sigma_x\tau_x + k_y\sigma_0\tau_y\right) + \left[M - \xi\left(k_x^2 + k_y^2\right) + \xi_z k_z^2\right]\sigma_0\tau_z + \mathscr{H}_U, \quad (1)$$

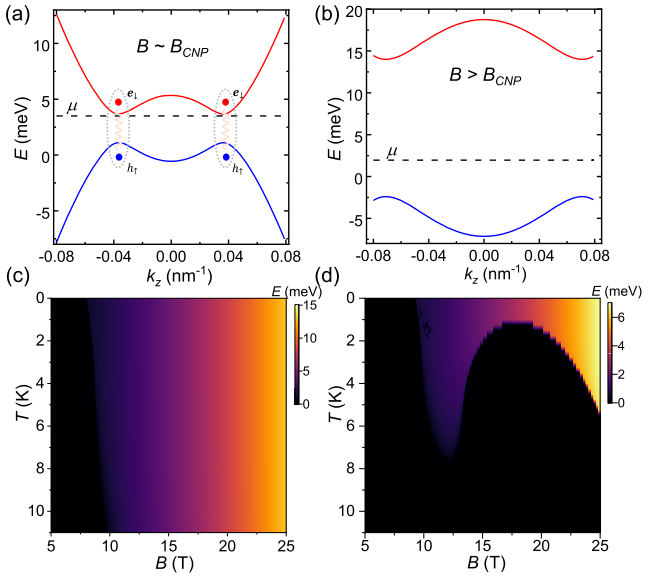

FIG. 4. (a), (b) Low-energy excitation spectrum of the gapped 1D Weyl nodes, with the chemical potential (μ) located approaching the gap in (a) and staying inside the gap in (b). As B increases, electrons and holes from the zeroth Landau bands form excitons and condense, leading to a gap opening. The system maintains charge neutrality after the exciton condensation. (c), (d) Temperature-magnetic-field phase diagram for the excitonic insulator phase calculated with two representative dielectric constant values, $\epsilon_r = 25$ for (c) and $\epsilon_r = 32.8$ for (d). The exciton gap size is shown with the color scale.

where σ and τ act on spin and orbital degrees of freedom, and $\mathscr{H}_U$ denotes the Coulomb interaction. For B along the z direction, the orbital contribution in the $\mu = x$, y plane can be taken into account through a minimal coupling $k_\mu \to -i\hbar\partial_\mu - (e/c)A_\mu$. The Zeeman energy is $\mathscr{H}_z = -\frac{1}{2}g_1\mu_B B\sigma_z - \frac{1}{2}g_2\mu_B B\sigma_z\tau_z$, where the g_2 term accounts for the disparity of the g factor for the two orbitals. The orbital coupling quantizes the electron motion in the x-y plane into LLs, and only the momentum k_z remains a good quantum number. In the QL, the dispersions for the zeroth LBs where all electrons reside contain an electron band with spin-up and a hole band with spin-down. The effective Hamiltonians take a simple form $\mathscr{H}_{\mathrm{eff}} = (\xi_z k_z^2 + m_c)c^\dagger c + (-\xi_z k_z^2 + m_h)h^\dagger h + \mathscr{H}_U$. One salient feature of $\mathscr{H}_{\mathrm{eff}}$ is that the electron (with creation operator $c^\dagger$) and hole branch (with creation operator $h^\dagger$) have the same band mass, and therefore it is expected that the particle-hole susceptibility dominates other instabilities such as the inter-Weyl node instabilities. With Coulomb interaction, the system opens a gap by developing the exciton instability associated with the order parameter $\Delta = \langle c_k^\dagger h_k\rangle$. Since h_k/c_k has spin-down and -up, Δ has spin quantum one and does not have center-of-mass momentum. Therefore, the resulting EI is a triplet exciton preserving the translation symmetry. The triplet exciton

can coexist with higher fields than the conventional singlet exciton.

The results of detailed model calculations of Eq. (1) are presented in Fig. 4 and Supplemental Material [43]. In the QL, as we increase B, the 0^+ and 0^- LLs move toward each other as a consequence of opposite spin polarization and form a 1D Weyl mode, consistent with the experimental observation of NLMR in S2. Concomitantly, μ is lowered from the 0^- LL due to the increased LLs degeneracy and approaches the band edge of the 0^+ LL. At low temperatures, the spin-triplet exciton opens a gap $\Delta \neq 0$ in the spectrum, which evolves with the magnetic field. The T-B phase diagram for the exciton phase is displayed in Figs. 4(c) and 4(d) for the cases with different dielectric constant. The triplet excitonic phase shrinks when the Coulomb interaction is suppressed (also shown in Fig. S11 of Supplemental Material [43]), i.e., in higher carrier-density systems associated with higher dielectric constant due to enhanced screening. At higher fields, the EI becomes unstable as μ shifts away from the Weyl node region. However, for a strong Coulomb interaction, the EI phase persists to high fields. Deep in the EI phase, the electron and hole carriers are compensated, resulting in a vanishing Hall conductivity, which is consistent with the experimental observation of a zero Hall conductivity, as shown in Fig. 3(d).

One important manifestation of the exciton phase is the nonlinear electrical transport. At zero temperature and a small bias voltage, the current vanishes because excitons are charge neutral. When the voltage exceeds a threshold value, excitons are dissolved, and the current jumps to a finite value [51]. At nonzero temperatures, the jump in current is smeared out by thermal fluctuations. The results shown in Fig. 6 align well with the EI picture (see Appendix B).

Discussion—Excitonic states have been reported in systems such as bilayer structures [52–55], monolayer tellurides [56–59], 1T-$TiSe_2$, and Ta_2NiSe_5 [60,61], often without the need for magnetic fields. In these materials, excitonic order often coexists with charge-density-wave phases, making it challenging to distinguish between the two. This has motivated the search for excitonic materials with valence and conduction bands located at the Brillouin zone center, with a direct gap, avoiding CDW coexistence [62]. Additionally, materials with spin-polarized valence and conduction bands have been predicted to host spin-triplet EIs [39–41], though experimental confirmation remains elusive. $HfTe_5$, with its small Dirac gap centered at the Γ point, provides a promising platform to explore spin-triplet EIs in the ultra-QL, as only the spin-polarized 0^- and 0^+ LBs are populated, as illustrated in Fig. 1(a). As B increases, the Fermi wave vector of the electron or hole states overlap at the same momenta, resembling the behavior of a direct-band-gap semiconductor. This contrasts with materials like graphite, where carrier pairs exhibit nonzero average momentum at high fields, resembling an indirect-band-gap semiconductor [14]. In graphite, the EI phase emerges under high fields [12,14,63–65], with distinct phases identified based on degeneracy lifting in the zeroth and first LLs [64].

At the CNP, electron- and holelike carriers coexist in the LLs, providing favorable conditions for EI formation [66,67]. While a competing CDW phase could form by condensing electron-hole pairs, it would result in continuous Hall conductivity variations with B, inconsistent with our observation of vanishing Hall conductivity over a wide field range. Furthermore, the direct-gap nature of $HfTe_5$ disfavors CDW formation [68]. Sample S3 showed the lowest carrier density and at the same time showed the clearest $\rho_{xy} = 0$ of all samples. We believe samples S1 and S2 showed nonperfect charge compensation with a weaker EI phase, as demonstrated by our simulations in Figs. 4(c) and 4(d) where the sample carrier density and dielectric constant affect the EI gap formation. Even more, the temperature dependence of B_{CNP} in S3 [Fig. 3(b) inset and Supplemental Material Fig. S8(b) [43]] fits well to a BCS-like model including pair-breaking effects, further supporting the EI scenario.

The spin-triplet EI phase in $HfTe_5$ is analogous to that in the quantum Hall bilayers [69], where excitons form between electrons and holes in LLs. In this case, the layer pseudospin of quantum Hall bilayers is replaced by the physical spin of the excitons, opening possibilities for future studies of phenomena such as Coulomb drag with spin-polarized currents and Josephson-like tunneling effects.

Conclusions—In conclusion, our magnetotransport experiments under high fields on $HfTe_5$, combined with the material-specific modeling, uncover novel emergent quantum phases inherent to its unique topological nature. $HfTe_5$ in the ultra-QL exhibits a simple band structure where μ intersects only the spin-polarized zeroth LBs. With increasing B, these bands cross, forming a 1D Weyl phase, evidenced by the NLMR. With further enhanced confinement of the 1D electron liquid by B, we observe a metal-to-insulator transition associated with a gap opening ($\sim$250 μeV). Furthermore, the persistence of a charge-neutral insulating state up to $B = 72$ T suggests the formation of a correlated phase consistent with a spin-triplet BCS-like EI. Material-specific modeling supports this interpretation, with additional evidence provided by the nonlinear I-V measurements. Our results reveal the formation of a spin-triplet excitonic insulator phase in the ultra-QL of $HfTe_5$ distinguished by its pairing of oppositely spin-polarized electrons and holes at equal momenta. Unlike conventional singlet excitonic insulators, the triplet state preserves translational symmetry and is potentially more robust under extreme conditions. This discovery paves the way for exploring emergent spin transport phenomena, including spin superfluidity and Josephson-like tunneling, with possible applications in spin-based quantum devices.

Acknowledgments—This research was primarily supported by the Laboratory Directed Research and Development program of Los Alamos National Laboratory under Project No. 20230014DR. This research was partially supported by the National Science Foundation Materials Research Science and Engineering Center program through the UC Irvine Center for Complex and Active Materials (Grant No. DMR-2011967). L. A. J. acknowledges the support from NSF-CAREER (Grant No. DMR 2146567). This work was performed, in part, at the Center for Integrated Nanotechnologies, an Office of Science User Facility operated by the U.S. Department of Energy Office of Science. Los Alamos National Laboratory, an affirmative action equal opportunity employer, is managed by Triad National Security, LLC for the U.S. Department of Energy's NNSA, under Contract No. 89233218CNA000001. A portion of this work was performed at the National High Magnetic Field Laboratory, which is supported by National Science Foundation Cooperative Agreements No. DMR-1644779 and No. DMR-2128556, the State of Florida, and the U.S. Department of Energy. J. L. and L. A. J. are grateful to Javier Sanchez-Yamagishi and his group at UCI for the initial measurements at low magnetic fields in his laboratory. We thank Qiyin Lin for assistance with the metal evaporation using the Angstrom *e*-beam evaporator at the UC Irvine Materials Research Institute and Matthew Law and Geemin Kim for helping us using their thermal metal evaporator. J. L. would like to thank Yi-Xiang Wang at Jiangnan University and Xiang Yuan at East China Normal University for fruitful discussions. We thank Pulsed Field Facility staff Johanna Palmstrom for discussing the data.

J. L. and V. S. contributed equally to this work.

[1] E. Y. Andrei, G. Deville, D. C. Glattli, F. I. B. Williams, E. Paris, and B. Etienne, Phys. Rev. Lett. **60**, 2765 (1988).
[2] H. Fukuyama, P. M. Platzman, and P. W. Anderson, Phys. Rev. B **19**, 5211 (1979).
[3] D. Yoshioka and P. A. Lee, Phys. Rev. B **27**, 4986 (1983).
[4] Y. Kuramoto and C. Horie, Solid State Commun. **25**, 713 (1978).
[5] L. V. Butov, A. Zrenner, G. Abstreiter, G. Böhm, and G. Weimann, Phys. Rev. Lett. **73**, 304 (1994).
[6] D. C. Tsui, H. L. Stormer, and A. C. Gossard, Phys. Rev. Lett. **48**, 1559 (1982).
[7] R. B. Laughlin, Phys. Rev. Lett. **50**, 1395 (1983).
[8] A. W. Overhauser, Phys. Rev. **167**, 691 (1968).
[9] B. I. Halperin, Jpn. J. Appl. Phys. **26**, 1913 (1987).
[10] Y. Iye, P. M. Tedrow, G. Timp, M. Shayegan, M. S. Dresselhaus, G. Dresselhaus, A. Furukawa, and S. Tanuma, Phys. Rev. B **25**, 5478 (1982).
[11] H. Yaguchi and J. Singleton, Phys. Rev. Lett. **81**, 5193 (1998).
[12] D. V. Khveshchenko, Phys. Rev. Lett. **87**, 246802 (2001).
[13] F. Arnold, A. Isidori, E. Kampert, B. Yager, M. Eschrig, and J. Saunders, Phys. Rev. Lett. **119**, 136601 (2017).
[14] K. Akiba, A. Miyake, H. Yaguchi, A. Matsuo, K. Kindo, and M. Tokunaga, J. Phys. Soc. Jpn. **84**, 054709 (2015).
[15] K. Behnia, L. Balicas, and Y. Kopelevich, Science **317**, 1729 (2007).
[16] P. J. W. Moll, A. C. Potter, N. L. Nair, B. J. Ramshaw, K. A. Modic, S. Riggs, B. Zeng, N. J. Ghimire, E. D. Bauer, R. Kealhofer, F. Ronning, and J. G. Analytis, Nat. Commun. **7**, 12492 (2016).
[17] C.-L. Zhang *et al.*, Nat. Phys. **13**, 979 (2017).
[18] B. J. Ramshaw, K. A. Modic, A. Shekhter, Y. Zhang, E.-A. Kim, P. J. W. Moll, M. D. Bachmann, M. K. Chan, J. B. Betts, F. Balakirev, A. Migliori, N. J. Ghimire, E. D. Bauer, F. Ronning, and R. D. McDonald, Nat. Commun. **9**, 2217 (2018).
[19] S. Liang, S. Kushwaha, T. Gao, M. Hirschberger, J. Li, Z. Wang, K. Stolze, B. Skinner, B. A. Bernevig, R. J. Cava, and N. P. Ong, Nat. Mater. **18**, 443 (2019).
[20] S. Li, C. M. Wang, Z. Z. Du, F. Qin, H.-Z. Lu, and X. C. Xie, npj Quantum Mater. **6**, 96 (2021).
[21] J. Gooth, S. Galeski, and T. Meng, Rep. Prog. Phys. **86**, 044501 (2023).
[22] Q. Li, D. E. Kharzeev, C. Zhang, Y. Huang, I. Pletikosić, A. V. Fedorov, R. D. Zhong, J. A. Schneeloch, G. D. Gu, and T. Valla, Nat. Phys. **12**, 550 (2016).
[23] T. Liang, J. Lin, Q. Gibson, S. Kushwaha, M. Liu, W. Wang, H. Xiong, J. A. Sobota, M. Hashimoto, P. S. Kirchmann, Z.-X. Shen, R. J. Cava, and N. P. Ong, Nat. Phys. **14**, 451 (2018).
[24] F. Tang, Y. Ren, P. Wang, R. Zhong, J. Schneeloch, S. A. Yang, K. Yang, P. A. Lee, G. Gu, Z. Qiao, and L. Zhang, Nature (London) **569**, 537 (2019).
[25] Y. Liu, H. Wang, H. Fu, J. Ge, Y. Li, C. Xi, J. Zhang, J. Yan, D. Mandrus, B. Yan, and J. Wang, Phys. Rev. B **103**, L201110 (2021).
[26] J. Ge, D. Ma, Y. Liu, H. Wang, Y. Li, J. Luo, T. Luo, Y. Xing, J. Yan, D. Mandrus, H. Liu, X. C. Xie, and J. Wang, Natl. Sci. Rev. **7**, 1879 (2020).
[27] P. Wang, Y. Ren, F. Tang, P. Wang, T. Hou, H. Zeng, L. Zhang, and Z. Qiao, Phys. Rev. B **101**, 161201(R) (2020).
[28] S. Galeski, X. Zhao, R. Wawrzyńczak, T. Meng, T. Förster, P. M. Lozano, S. Honnali, N. Lamba, T. Ehmcke, A. Markou, Q. Li, G. Gu, W. Zhu, J. Wosnitza, C. Felser, G. F. Chen, and J. Gooth, Nat. Commun. **11**, 5926 (2020).
[29] W. Wu, Z. Shi, Y. Du, Y. Wang, F. Qin, X. Meng, B. Liu, Y. Ma, Z. Yan, M. Ozerov, C. Zhang, H.-Z. Lu, J. Chu, and X. Yuan, Nat. Mater. **22**, 84 (2023).
[30] Z. Cai and Y.-X. Wang, Phys. Rev. B **108**, 155202 (2023).
[31] P.-L. Zhao, J. L. Zhang, H.-Z. Lu, and Q. Niu, arXiv:2409.07199.
[32] Y. Zhang, Q. Li, P. Zhao, Y. Qian, Y. Lv, Y. Chen, Q. Niu, H. Lu, J. Zhang, and M. Tian, arXiv:2410.11154.
[33] S. Galeski, H. F. Legg, R. Wawrzyńczak, T. Förster, S. Zherlitsyn, D. Gorbunov, M. Uhlarz, P. M. Lozano, Q. Li, G. D. Gu, C. Felser, J. Wosnitza, T. Meng, and J. Gooth, Nat. Commun. **13**, 7418 (2022).
[34] A. Imambekov, T. L. Schmidt, and L. I. Glazman, Rev. Mod. Phys. **84**, 1253 (2012).
[35] D. Jérome, T. M. Rice, and W. Kohn, Phys. Rev. **158**, 462 (1967).
[36] M. Sigrist and K. Ueda, Rev. Mod. Phys. **63**, 239 (1991).

[37] V. Crépel and L. Fu, Proc. Natl. Acad. Sci. U.S.A. **119**, e2117735119 (2022).
[38] A. J. Leggett, Rev. Mod. Phys. **47**, 331 (1975).
[39] Z. Jiang, W. Lou, Y. Liu, Y. Li, H. Song, K. Chang, W. Duan, and S. Zhang, Phys. Rev. Lett. **124**, 166401 (2020).
[40] A. Ikeda, Y. H. Matsuda, K. Sato, Y. Ishii, H. Sawabe, D. Nakamura, S. Takeyama, and J. Nasu, Nat. Commun. **14**, 1744 (2023).
[41] H. Yang, J. Zeng, Y. Shao, Y. Xu, X. Dai, and X.-Z. Li, Phys. Rev. B **109**, 075167 (2024).
[42] J. Liu, Y. Zhou, S. Yepez Rodriguez, M. A. Delmont, R. A. Welser, T. Ho, N. Sirica, K. McClure, P. Vilmercati, J. W. Ziller, N. Mannella, J. D. Sanchez-Yamagishi, M. T. Pettes, R. Wu, and L. A. Jauregui, Nat. Commun. **15**, 332 (2024).
[43] See Supplemental Material at http://link.aps.org/supplemental/10.1103/bj2n-4k2w for experimental methods, more experimental data and discussions, and details of theoretical modeling.
[44] H. Yaguchi, Y. Iye, T. Takamasu, N. Miura, and T. Iwata, J. Phys. Soc. Jpn. **68**, 1300 (1999).
[45] F. Qin, S. Li, Z. Z. Du, C. M. Wang, W. Zhang, D. Yu, H.-Z. Lu, and X. C. Xie, Phys. Rev. Lett. **125**, 206601 (2020).
[46] A. Gourgout, M. Leroux, J.-L. Smirr, M. Massoudzadegan, R. P. S. M. Lobo, D. Vignolles, C. Proust, H. Berger, Q. Li, G. Gu, C. C. Homes, A. Akrap, and B. Fauqué, npj Quantum Mater. **7**, 71 (2022).
[47] E. Martino, I. Crassee, G. Eguchi, D. Santos-Cottin, R. D. Zhong, G. D. Gu, H. Berger, Z. Rukelj, M. Orlita, C. C. Homes, and A. Akrap, Phys. Rev. Lett. **122**, 217402 (2019).
[48] Y. Jiang, J. Wang, T. Zhao, Z. L. Dun, Q. Huang, X. S. Wu, M. Mourigal, H. D. Zhou, W. Pan, M. Ozerov, D. Smirnov, and Z. Jiang, Phys. Rev. Lett. **125**, 046403 (2020).
[49] J. Wang, Y. Jiang, T. Zhao, Z. Dun, A. L. Miettinen, X. Wu, M. Mourigal, H. Zhou, W. Pan, D. Smirnov, and Z. Jiang, Nat. Commun. **12**, 6758 (2021).
[50] Z. Rukelj, C. C. Homes, M. Orlita, and A. Akrap, Phys. Rev. B **102**, 125201 (2020).
[51] Y. Shao and X. Dai, Phys. Rev. X **14**, 021047 (2024).
[52] J. P. Eisenstein and A. H. MacDonald, Nature (London) **432**, 691 (2004).
[53] X. Liu, J. I. A. Li, K. Watanabe, T. Taniguchi, J. Hone, B. I. Halperin, P. Kim, and C. R. Dean, Science **375**, 205 (2022).
[54] R. Wang, T. A. Sedrakyan, B. Wang, L. Du, and R.-R. Du, Nature (London) **619**, 57 (2023).
[55] L. Ma, P. X. Nguyen, Z. Wang, Y. Zeng, K. Watanabe, T. Taniguchi, A. H. MacDonald, K. F. Mak, and J. Shan, Nature (London) **598**, 585 (2021).
[56] Y. Jia *et al.*, Nat. Phys. **18**, 87 (2022).
[57] Y. Song, C. Jia, H. Xiong, B. Wang, Z. Jiang, K. Huang, J. Hwang, Z. Li, C. Hwang, Z. Liu, D. Shen, J. A. Sobota, P. Kirchmann, J. Xue, T. P. Devereaux, S.-K. Mo, Z.-X. Shen, and S. Tang, Nat. Commun. **14**, 1116 (2023).
[58] Q. Gao, Y. Chan, Y. Wang, H. Zhang, P. Jinxu, S. Cui, Y. Yang, Z. Liu, D. Shen, Z. Sun, J. Jiang, T. C. Chiang, and P. Chen, Nat. Commun. **14**, 994 (2023).
[59] B. Sun, W. Zhao, T. Palomaki, Z. Fei, E. Runburg, P. Malinowski, X. Huang, J. Cenker, Y.-T. Cui, J.-H. Chu, X. Xu, S. S. Ataei, D. Varsano, M. Palummo, E. Molinari, M. Rontani, and D. H. Cobden, Nat. Phys. **18**, 94 (2022).
[60] H. M. Bretscher, P. Andrich, Y. Murakami, D. Golež, B. Remez, P. Telang, A. Singh, L. Harnagea, N. R. Cooper, A. J. Millis, P. Werner, A. K. Sood, and A. Rao, Sci. Adv. **7**, eabd6147 (2021).
[61] A. Kogar, M. S. Rak, S. Vig, A. A. Husain, F. Flicker, Y. I. Joe, L. Venema, G. J. MacDougall, T. C. Chiang, E. Fradkin, J. van Wezel, and P. Abbamonte, Science **358**, 1314 (2017).
[62] S. Wu, L. M. Schoop, I. Sodemann, R. Moessner, R. J. Cava, and N. P. Ong, Nature (London) **635**, 301 (2024).
[63] Z. Zhu, R. D. McDonald, A. Shekhter, B. J. Ramshaw, K. A. Modic, F. F. Balakirev, and N. Harrison, Sci. Rep. **7**, 1733 (2017).
[64] Z. Zhu, P. Nie, B. Fauqué, B. Vignolle, C. Proust, R. D. McDonald, N. Harrison, and K. Behnia, Phys. Rev. X **9**, 011058 (2019).
[65] J. Wang, P. Nie, X. Li, H. Zuo, B. Fauqué, Z. Zhu, and K. Behnia, Proc. Natl. Acad. Sci. U.S.A. **117**, 30215 (2020).
[66] J. Zang, J. Wang, J. Cano, and A. J. Millis, Phys. Rev. B **104**, 075150 (2021).
[67] P. Tscheppe, J. Zang, M. Klett, S. Karakuzu, A. Celarier, Z. Cheng, C. A. Marianetti, T. A. Maier, M. Ferrero, A. J. Millis, and T. Schäfer, Proc. Natl. Acad. Sci. U.S.A. **121**, e2311486121 (2024).
[68] P. Zhang, Y. Dong, D. Yan, B. Jiang, T. Yang, J. Li, Z. Guo, Y. Huang, Haobo, Q. Li, Y. Li, K. Kurokawa, R. Wang, Y. Nie, M. Hashimoto, D. Lu, W.-H. Jiao, J. Shen, T. Qian, Z. Wang, Y. Shi, and T. Kondo, Phys. Rev. X **14**, 011047 (2024).
[69] J. P. Eisenstein, Annu. Rev. Condens. Matter Phys. **5**, 159 (2014).
[70] C. Zhang, J. Yang, Z. Yan, X. Yuan, Y. Liu, M. Zhao, A. Suslov, J. Zhang, L. Pi, Z. Wang, and F. Xiu, Natl. Sci. Rev. **9**, nwab208 (2022).
[71] A. N. Kozlov and L. A. Maksimov, Sov. J. Exp. Theor. Phys. **21**, 790 (1965).
[72] L. V. Keldysh and Y. V. Kopaev, Sov. Phys. Solid State **6**, 2219 (1965).

End Matter

Appendix A: Magnetic-field-induced metal-to-insulator transition—Pulsed magnetic field measurements on sample S3 reveal the evolution of ρ_{xx} vs T at various B, as shown in Fig. 5(a). At $B = 5$ T, ρ_{xx} increases slightly with increasing T, displaying metallic transport behavior. However, for $B > 7.5$ T, ρ_{xx} decreases strongly with increasing T, indicating semiconductorlike transport behavior. From Arrhenius fitting, the magnetic field dependence of the thermal activation gap is shown in Fig. 3(c).

We further calculate $B\sigma_{xy}/e$, which corresponds to the carrier density difference between electrons and holes

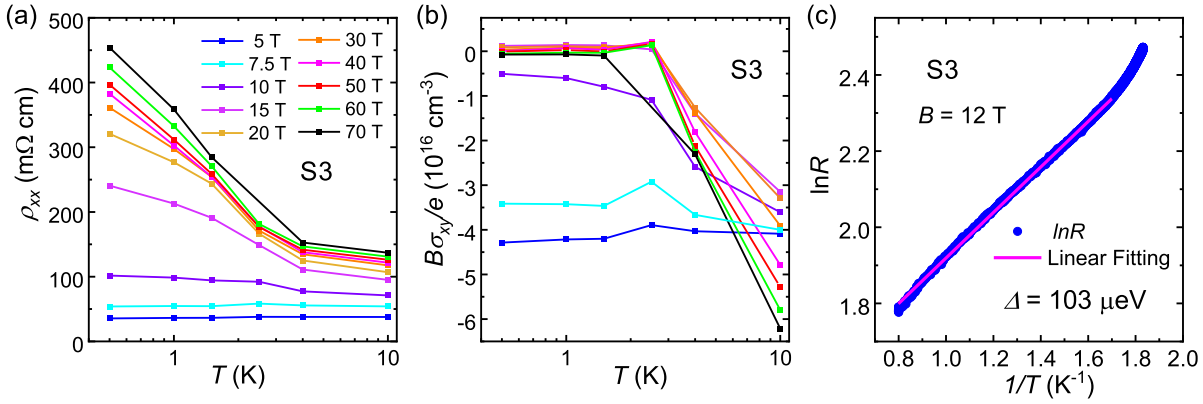

FIG. 5. (a) ρ_{xx} at various magnetic fields ($B = 5$, 7.5, 15, 20, 30, 40, 50, 60, and 70 T) plotted as functions of the temperature (T) with the x axis in log scale for S3. (b) $B\rho_{xy}/e$ with a unit of cm^{-3} at the same magnetic fields as those of (a) plotted as functions of T. (c) ln R_{xx} ($B = 12$ T) plotted against $1/T$ measured in a superconducting magnet and the Arrhenius fitting, resulting a thermal activation gap of 103 μeV.

($n_e - n_h = B\sigma_{xy}/e$) for the corresponding magnetic fields shown in Fig. 5(a). The temperature dependence of $B\sigma_{xy}/e$ at various magnetic fields is then plotted in Fig. 5(b). At $T = 10$ K, $B\sigma_{xy}/e$ is always negative for all magnetic fields, indicating electron-dominated transport. At $B = 5$ and 7.5 T, when the transport is still metallic, $B\sigma_{xy}/e$ shows a weak temperature dependence. At $B = 10$ T, a magnetic field approaching B_{CNP}, $B\sigma_{xy}/e$ increases progressively with lowering T, and tends to saturate at a finite negative value down to $T = 0.5$ K. The electronlike net carrier density changes from 3.1×10^{16} cm^{-3} at $T = 10$ K to 0.5×10^{16} cm^{-3} at $T = 0.5$ K. However, for $B > B_{\mathrm{CNP}}$, $B\sigma_{xy}/e$ systematically shifts from negative values at high temperatures to a small value around zero (within an accuracy of $\pm 0.1 \times 10^{16}$ cm^{-3}) at $T < 2$ K, up to $B = 70$ T, indicating charge-neutral transport in the system.

To further verify the insulating gap, with a higher precision, we have performed electrical transport measurements on S3 in a superconducting magnet up to 12 T. The temperature dependence of R_{xx} measured at $B = 12$ T is given in Fig. 5(c). From the Arrhenius analysis, we extracted a thermal activation gap $\Delta = 103$ μeV. This gap measured by slow cooling at a constant magnetic field agrees well with the gap extracted from the pulsed magnetic field experiments as shown in the inset of Fig. 3(c).

Appendix B: Nonlinear electrical transport—Even though the correlated gap is not fully developed at $B = 12$ T, nonlinear electrical transport is still observed in S3, as measured in a superconducting magnet depicted in Fig. 6. Figure 6(a) shows the dc current vs voltage (I-V) curves, and Fig. 6(b) shows dV/dI vs I_{dc} measured under different magnetic fields at $T = 0.55$ K. At $B = 0$ and 5 T, dV/dI remains constant with increasing bias dc current (I_{dc}), and the I-V is linear. For $B > 6$ T, however, dV/dI vs I_{dc} displays a prominent peak around zero bias current and the I-Vs show nonlinear behaviors; i.e., the conductance is small at low bias voltages and increases as the dc voltage increases. This nonlinear transport behavior is magnetic field dependent and becomes stronger with increasing field.

Figures 6(c) and 6(d) show the evolution of dV/dI vs I_{dc} and I-Vs at different temperatures and $B = 12$ T. The dV/dI peak is weakened progressively with increasing temperature. The I-Vs gradually evolve from nonlinear to linear behavior with increasing temperature, and the nonlinearity is barely discernible at $T = 1.25$ K. This

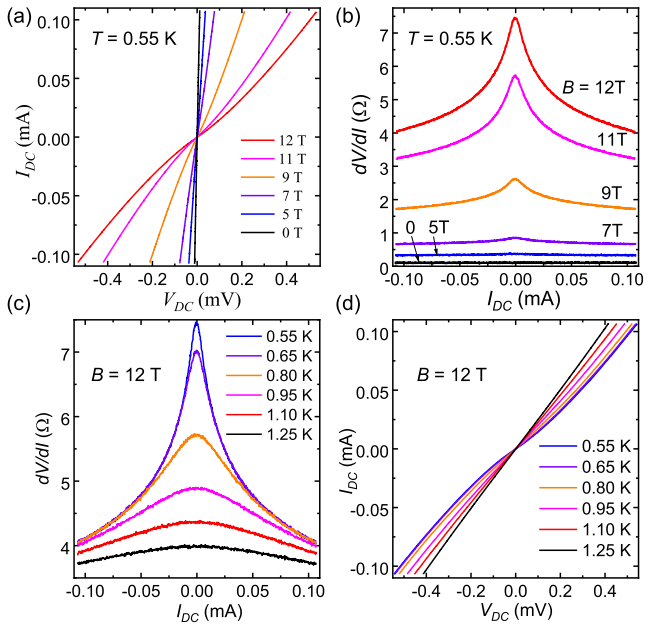

FIG. 6. (a),(b) Current vs voltage (I-V) and dV/dI plotted as a function of dc current (I_{dc}), respectively, measured at $T = 0.55$ K and different representative B's for S3 in a superconducting magnet. (c) dV/dI vs I_{dc} for S3 measured at $B = 12$ T and various temperatures. (d) I-V curves for the measurements in (c).

temperature evolution highlights the melting of the insulating state with increasing temperatures. Our nonlinear transport results confirm a gap formation for $B > B_C$, while also suggesting the need for further investigation into the electrical breakdown behavior of the excitonic insulator phase with enhanced gap size in the ultra-quantum limit of $HfTe_5$. We note that the peak observed in our dV/dI vs I_{dc} measurement decays monotonically with increasing bias, which is different from the dip or peak features caused by the sliding motion of density waves as previously seen in higher density samples of $HfTe_5$ [70].

Appendix C: Coulomb interaction and excitonic insulator gap—When the chemical potential intersects both the electron and hole zeroth Landau bands, the system hosts coexisting electronlike and holelike carriers. The Coulomb interaction between these carriers can drive the formation of the EI phase through the opening of the gap Δ in the spectrum [35,71,72]. The effective Hamiltonian describing this interaction can be modeled as $\mathscr{H}_{\text{eff}} = \sum_k (\xi_z k_z^2 + m_c) c_k^\dagger c_k + (-\xi_z k_z^2 + m_h) h_k^\dagger h_k - V_0 \sum_{k,k'} c_k^\dagger h_k c_{k'} h_{k'}^\dagger$, where c_k and h_k are the electron and hole operators, respectively. In this Letter, the gap is estimated analogous to the BCS theory of superconductivity by self-consistently solving the gap equation $\Delta = V_0 \sum_k \langle c_k h_k^\dagger \rangle$. The resulting gapped states and phase diagram are shown in Figs. 4(c) and 4(d). In our calculations, it is assumed that the chemical potential is not significantly altered by the temperature in the ranges under consideration. It is also assumed that the chemical potential is not significantly changed by the condensation. These assumptions are valid for low temperatures in the regime where $\Delta \ll \mu$.

Finally, the Coulomb interaction is approximated as $V_0 = (1/4\pi\epsilon_0\epsilon_r)(e^2/a)$, where $a \sim (n_0)^{-1/3}$ is the average interparticle distance, and ϵ_r is the dielectric constant. Since higher carrier densities lead to larger ϵ_r, the effective interaction weakens with increasing density, reducing the excitonic gap and suppressing the EI phase. Figure 4 and Supplemental Material Fig. S11 [43] depict the calculated phase diagram for different values of ϵ_r, highlighting the impact of dielectric screening (carrier density) on gap formation.